

## Scientific paper

# Mesoscopic Simulation of Failure of Mortar and Concrete by 3D RBSM

Kohei Nagai<sup>1</sup>, Yasuhiko Sato<sup>2</sup> and Tamon Ueda<sup>3</sup>

Received 26 April 2005, accepted 2 July 2005

## Abstract

Concrete is a heterogeneous material consisting of mortar and aggregate at the meso scale. Evaluation of the fracture process at this scale is useful to clarify the material characteristic of concrete. The authors have conducted meso scale analysis of concrete over a past few years by Rigid Body Spring Model (RBSM). In this study, three-dimensional analyses of mortar and concrete are carried out, which is necessary for the quantitative evaluation of concrete behavior especially in compression. Constitutive models at the meso scale are developed for the 3D RBSM analysis. Failure behaviors and strengths in compression and tension of mortar and concrete are predicted well by the analysis. In biaxial compression test of concrete, crack in normal direction to plane of specimen is simulated that cannot be presented by two-dimensional analysis.

## 1. Introduction

The mesoscopic simulation of concrete, where the concrete is dealt as heterogeneous material, can be an efficient tool to estimate the behavior in various concretes such as fiber reinforced concrete and concrete deteriorated by environmental actions besides ordinary concrete. It is because the composing materials themselves are modeled in the analyzed concrete, considering the mechanical properties of each component and interface between the components. Deterioration mechanism by environmental action is often described at the meso scale. Much experimental research has been conducted on fracture mechanisms at the meso level in the past. In recent years, research at the meso level from the analytical point of view has begun but has yet been conducted far enough.

The authors have conducted the simulation of failure of concrete at meso scale where the concrete consists of mortar and aggregate by two-dimensional Rigid Body Spring Model (2D RBSM) (Nagai *et al.* 2004). The RBSM is one of the discrete analysis methods. Compared with common methods such as the Distinct Element Method (Cundall and Strack 1979), it is a suitable method for static and small deformation problems because the RBSM does not consider a re-contact of an element with neighbor elements other than the element where the springs are set initially between them. Therefore it has an advantage that reconstruction of stiffness

matrix in each step that increases the calculation time is not necessary. By the 2D RBSM analysis, the behavior of mortar and concrete under uniaxial stress condition as well as the relationship between compression and tension strengths is predicted well. However the analysis cannot simulate the behavior of concrete in biaxial compression test because the crack in normal direction to the biaxial stress plane, which is the primary cause of the failure, cannot be presented by two-dimensional analysis. It can be simulated by only three-dimensional analysis. And in two-dimensional analysis, the aggregates are presented by cylinders that extend through the thickness of the model therefore the complicated inside stress condition and three-dimensional fracture propagation of actual concrete cannot be simulated. The two-dimensional analysis is useful mainly to predict the behavior qualitatively. Furthermore, to predict the effect of environment on concrete material and reinforced concrete in the future, three-dimensional analysis is indispensable. Some environmental effects proceed from the concrete surface so that the corner part deteriorates first. Cracks in concrete caused by the corrosion of steel bar are likely to propagate three-dimensionally because the corrosion takes place differently at different location along the bar.

Three-dimensional analysis of concrete at meso scale has been hardly conducted especially in compression due to the complicated behavior. By Finite Element (FE) analysis, Wang and Chen conducted three-dimensional analysis under triaxial load (1998). Nagai *et al.* succeeded a development of meshing system for 3D FE analysis from the scanned image data of real concrete (1998, 2004). By the discrete analysis method, Lilliu and van Mier carried out the mesoscopic analysis of tension test of concrete by lattice type fracture model (2003). Though these large-scale DOF analyses have been conducted actively with the improvement of computer performance, the behavior of concrete has not been simulated reasonably in either compression or tension. Cusatis *et al.* applied the three-dimensional lattice type

<sup>1</sup>JSPS Post-doctoral Fellow, Institute of Structural Engineering, Swiss Federal Institute of Technology Zurich, Switzerland.

E-mail: kohei.nagai@ibk.baug.ethz.ch

<sup>2</sup>Associate Professor, Division of Built Environment, Hokkaido University, Japan.

<sup>3</sup>Professor, Division of Built Environment, Hokkaido University, Japan.

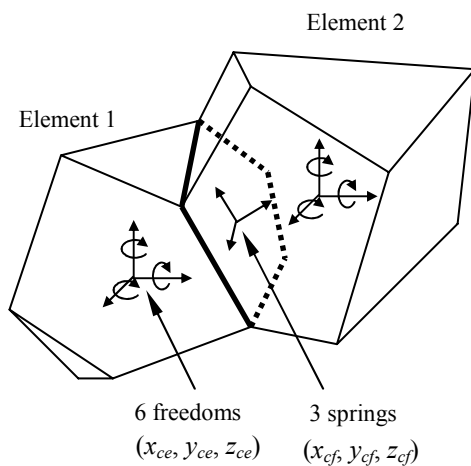
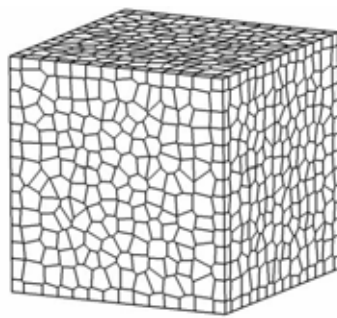
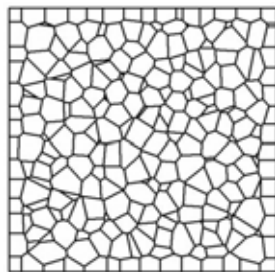


Fig.1 3D mechanical model.



a) 3D view



b) Cross section

Fig.2 3D Voronoi diagram.

model to the mesoscopic simulation of concrete material in various uniaxial and multi-axial stress conditions (2003a; 2003b). In the model, aggregates are connected by the lattice element that presents the material properties of aggregate and mortar. However the mortar element itself is not modeled in the analyses, which implies that the model may not simulate the precise fracture propagation inside the mortar.

In this study, three-dimensional numerical simulation of mortar and concrete at meso scale are carried out using the RBSM. Uniaxial and biaxial analyses are conducted and the failure process is discussed comparing to the two-dimensional analysis. With the three-dimensional RBSM (3D RBSM) analysis, Toi and Kiyosue have car-

ried out the research on damage mechanics model for brittle solids with micro cracking (1995). Simulation of concrete on three-dimension is conducted in recent years (Bolander and Berton 2004). However the mesoscopic analysis by 3D RBSM with large-scale DOF analysis has not been conducted yet.

## 2. Method of numerical analysis

The RBSM developed by Kawai and Takeuchi (Kawai 1978; Kawai and Takeuchi 1990) employs the discrete numerical analysis method. The analytical model is divided into polyhedron elements whose faces are interconnected by springs. Mechanical model of 3D RBSM is shown in Fig. 1. Each element has three transitional and three rotational degrees of freedom at a certain point within the element. The computational point  $(x_{ce}, y_{ce}, z_{ce})$  is defined as,

$$\begin{aligned} x_{ce} &= \frac{x_1 + x_2 + \cdots + x_i + \cdots + x_m}{m} \\ y_{ce} &= \frac{y_1 + y_2 + \cdots + y_i + \cdots + y_m}{m} \\ z_{ce} &= \frac{z_1 + z_2 + \cdots + z_i + \cdots + z_m}{m} \end{aligned} \quad (1)$$

where  $m$  is a number of node composing the element and  $x_i$ ,  $y_i$  and  $z_i$  are those coordinates. Three individual springs, which are one normal and two shear springs, are set at a point on the face between two elements. This point  $(x_{cf}, y_{cf}, z_{cf})$  is defined as,

$$\begin{aligned} x_{cf} &= \frac{x_1 + x_2 + \cdots + x_j + \cdots + x_n}{n} \\ y_{cf} &= \frac{y_1 + y_2 + \cdots + y_j + \cdots + y_n}{n} \\ z_{cf} &= \frac{z_1 + z_2 + \cdots + z_j + \cdots + z_n}{n} \end{aligned} \quad (2)$$

where  $n$  is a number of node composing the face and  $x_j$ ,  $y_j$  and  $z_j$  are those coordinates.

Since cracks initiate and propagate along the boundary face, the mesh arrangement may affect fracture direction. To avoid the formation of cracks in a certain direction, random geometry is introduced using a Voronoi diagram (Fig. 2). A Voronoi diagram is an assembly of Voronoi cells. Each cell represents a mortar or aggregate element in the analysis.

In the nonlinear analysis, a stiffness matrix is constructed based on the principle of virtual work (Kawai and Takeuchi 1990), and the Modified Newton-Raphson method is employed for the convergence algorithm. In the convergence process, displacements that cancel the unbalanced force of elements are added to the elements. The displacements are calculated using the stiffness matrix. Convergence of the model is judged when the ratio of  $\Sigma(\text{Unbalanced force of element in the model})^2$  to  $\Sigma(\text{Applied force to element})^2$  becomes less than  $10^{-5}$ .

When the model does not converge at a given maximum iterative calculation number, analysis proceeds to the next step. In the analysis, displacement of loading boundary is controlled. The simulation program is written in Fortran language and the analyses are conducted using a personal computer on Windows.

In the three-dimensional analysis, number of element and degrees of freedom of analyzed specimen are significantly larger than those in two-dimension. For example, the specimen of  $100 \times 100 \times 200$  mm contains 128,000 elements when the average size of element  $2.5\text{mm}^3$ . Degrees of freedom of the specimen become 768,000 where one element has six degrees of freedom. Meanwhile in two-dimensional analysis of  $100 \times 200$  mm specimen, when the average element size is  $2.5\text{mm}^2$ , the number of element and the degrees of freedom are 3,200 and 9,600, respectively, where one element has three degrees of freedom. Although Algebraic Multi-Grid (AMG) method, which is one of the known fast matrix solvers, is introduced to solve the huge matrix in three-dimensional analysis, the computational time is still long in nonlinear analysis adopted in this study. Then, the failure simulations of specimens with somewhat small size are conducted. The sizes are  $140 \times 70 \times 70$  mm in uniaxial test and  $140 \times 140 \times 35$  mm in biaxial test. The calculation time is reduced to around one week for one analysis.

In two-dimensional analysis of mortar and concrete, variation of analytical results is observed due to the random mesh arrangement and strength distribution (Nagai *et al.* 2004). The variation of strength is not examined thoroughly in the three-dimensional analysis in this paper because of the long simulation time. However, it has been confirmed that the variation is smaller than that in the two-dimension through some prior results of analyses.

### 3. Constitutive model

#### 3.1 Mortar model

In this study, a constitutive model for mortar at the meso scale is developed because a constitutive model at the macro scale cannot be applied to meso scale analysis.

The material characteristics of each component are

presented by means of modeling springs. In normal springs, compressive and tensile stresses ( $\sigma$ ) are developed. Shear springs develop shear stress ( $\tau$ ). The elastic modulus of normal spring ( $k_n$ ) and shear spring ( $k_s$ ) are presented assuming a plane strain condition,

$$k_n = \frac{(1 - \nu_{elem})E_{elem}}{(1 + \nu_{elem})(1 - 2\nu_{elem})} \quad (3)$$

$$k_s = \frac{E_{elem}}{1 + \nu_{elem}}$$

where  $k_n$  and  $k_s$  are the elastic modulus of normal and shear spring, and  $E_{elem}$  and  $\nu_{elem}$  are the corrected elastic modulus and Poisson's ratio of component at the meso scale, respectively. For calculation of shear stress, a resultant value of strains generated in two shear springs is adopted as a shear strain in the constitutive model presented in this chapter.

In the analysis, due to the nature of RBSM, the values of the material properties at the meso scale given to the elements are different from the material properties of the object analyzed at the macroscopic scale. In this study, the material properties for the elements were determined in such a way as to give the correct macroscopic properties. For this purpose, the elastic analysis of mortar in compression was carried out. In discrete analysis such as RBSM, the shape and fineness of elements affect analytical results (Nagai 2002). To reduce these effects, a small size for elements is adopted and element fineness in all the analyses is maintained to almost the same level. The volume of each element is approximately  $2.0 \sim 3.0 \text{ mm}^3$ . In the elastic analyses, the relationship between the macroscopic and mesoscopic Poisson's ratios and the effect of the mesoscopic Poisson's ratio on the macroscopic elastic modulus were examined. From the results (Fig. 3), Eqs. (4) and (5) are adopted for determining the mesoscopic material properties.

$$\nu_{elem} = -24.8\nu^4 + 31.9\nu^3 - 16.4\nu^2 + 4.28\nu \quad (4)$$

$$E_{elem} = (-33.7\nu_{elem}^4 + 17.0\nu_{elem}^3 - 4.13\nu_{elem}^2 + 0.327\nu_{elem} + 1)E \quad (5)$$

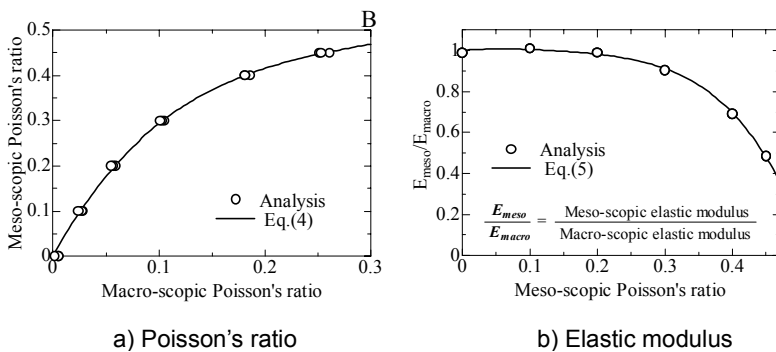


Fig. 3 Effect of mesoscopic material properties on macroscopic properties.

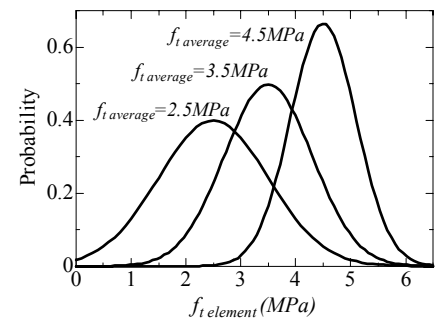


Fig. 4 Distribution of material properties.

where  $E$  and  $\nu$  are the macroscopic elastic modulus and Poisson's ratio of the analyzed object, respectively. It should be noted that these equations are introduced not to express the actual material properties at meso scale but to resolve the inherent problem of this analysis method.

Only the maximum tensile stress has to be set as a material strength. Actually, mortar itself is not a homogeneous material, which consists of sand, paste, air voids, and so on, even when the bleeding effect is ignored. This being heterogeneous can be considered by giving a strength distribution for mortar at meso scale. However the strength distribution in mortar has not been clarified yet. In this study, a normal distribution is assumed for the tensile strength on the element boundary. The probability density function is as follows (Fig. 4),

$$f(f_{t\text{elem}}) = \frac{1}{\sqrt{2\pi}\sigma} \exp\left\{-\frac{(f_{t\text{elem}} - \mu)^2}{2\sigma^2}\right\} \quad (6)$$

$$\mu = f_{t\text{average}}$$

$$\sigma = -0.2f_{t\text{average}} + 1.5$$

when  $f_{t\text{elem}} < 0$  then,  $f_{t\text{elem}} = 0$

where  $f_{t\text{elem}}$  is the distributed tensile strength and  $f_{t\text{average}}$  is the average tensile strength of mortar at the meso scale. The units of the tensile strengths are MPa in Eq (6). As seen in Eq. (6) and Fig. 4, the distribution varies according to the value of  $f_{t\text{average}}$ . Higher strength mortar is a more homogeneous material than lower strength mortar. This equation introduces our concept for the general tendency of mortar material properties. The same distribution applies to the elastic modulus, so that the elastic modulus for the element is multiplied by 1.05.

Springs set on the face behave elastically until stresses reach the  $\tau_{\max}$  criterion or tensile strength. The strains and stresses are calculated as follows.

$$\varepsilon = \frac{\delta_n}{h_1 + h_2} \quad (7)$$

$$\gamma = \frac{\delta_s}{h_1 + h_2}$$

$$\sigma = k_n \varepsilon$$

$$\tau = k_s \gamma$$

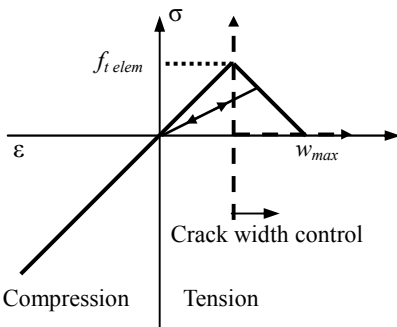


Fig. 5 Model of normal spring.

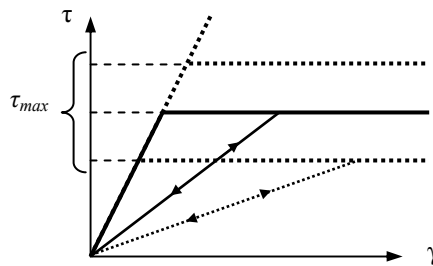


Fig. 6 Model of shear spring.

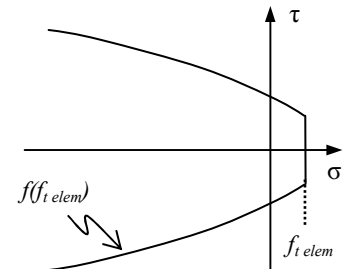


Fig. 7  $\tau_{\max}$  criterion for mortar.

where  $\varepsilon$  and  $\gamma$  are the strain of normal and shear springs.  $\delta_n$  and  $\delta_s$  are the normal and shear relative displacement of elements of those springs, respectively.  $h$  is the length of perpendicular line from the calculation point of element ( $x_{ce}, y_{ce}, z_{ce}$ ) to the boundary face. Subscripts 1 and 2 represent elements 1 and 2 in Fig. 1, respectively.

The constitutive model of a normal spring is shown in Fig. 5. In the compression zone, the spring always behaves elastically. Fracture happens between elements when the normal spring reaches tensile strength  $f_{t\text{elem}}$ , and the normal stress decreases linearly depending on the crack width, which corresponds to the spring elongation. In this study,  $w_{\max}$  is set 0.03 mm, which expresses more brittle behavior than the general macro scale concrete model. The linear unloading and reloading path that goes through the origin is introduced to the normal spring in the tension zone. For shear springs, an elasto plastic model is applied as shown in Fig. 6 in the range where normal springs do not fracture. The shear strain and the principal shear direction are determined from the resultant value of strains of two shear springs that are recalculated in each step. It means the principal shear direction may change every step. Since it is considered that the direction dose not change so much under the monotonic loading, the effect of changing in principal shear direction is not considered for simplicity. The value of  $\tau_{\max}$  changes depending on the condition of the normal spring and the tensile strength. The value of  $\tau_{\max}$  is given as follows (Fig. 7),

$$\tau_{\max} = \pm(0.30f_{t\text{elem}}^{2.5}(-\sigma + f_{t\text{elem}})^{0.4} + 0.15f_{t\text{elem}}) \quad (\sigma \leq f_{t\text{elem}}) \quad (8)$$

This criterion, which affects the result of analysis considerably, is originally developed for 3D RBMS meso-scale analysis. In the constitutive model for 2D RBMS developed by the authors, a different equation is adopted for the  $\tau_{\max}$  criterion (Nagai *et al.* 2004). The angles of face, where springs are set, vary in the  $z$  direction by the  $z$  coordinate in 3D analysis. In 2D analysis in  $x$ - $y$  direction, however, the faces on the  $z$  direction are represented by one face. As a result the generated stress condition is different between the 3D and 2D analyses even for the same displacements in the  $x$  and  $y$  directions. Hence the different constitutive models are necessary to

be applied.

When the tension fracture (or cracking) occurs in the normal spring, the calculated shear stress is reduced according to the reduction ratio of normal tensile stress. The shear spring cannot carry the shear stress when the crack width in the normal spring direction reaches  $w_{max}$ .

After the stresses reach the shear stress criterion, the stresses are transferred only through an over-wrapped part of the boundary faces between two elements, which is calculated by the elongation of the shear spring and the area of the face where the springs are set. In 3D analysis, calculation of over-wrapped area of the polygon faces is difficult therefore the over-wrapped area is calculated using circular faces equivalent to the polygon faces as shown in Fig. 8.

In the constitutive model, normal springs in compression only behave elastically and never break nor exhibit softening behavior.

### 3.2 Aggregate model

In this study, the effect of the existence of aggregate in concrete on the fracture process is examined. For this purpose, aggregate elements are assumed to behave only elastically without fracture in this study. The same equations as (3), (4), (5) and (7) are adopted to present the material property of aggregate.

### 3.3 Interface model

The behavior of interface between mortar and aggregate are presented by the spring between these elements. The same stress strain relationships as Eq. (7) and strength and stiffness distribution as Eq. (6) are adopted for the material properties of the interface between the mortar and aggregate. The spring stiffnesses  $k_n$  and  $k_s$  of the interface are given by a weighted average of the material properties in two elements according to their perpendiculars because it acts as the elastic composite material of mortar and aggregate before the crack occurrence or the yielding of shear spring, i.e.,

$$k_n = \frac{k_{n1}h_1 + k_{n2}h_2}{h_1 + h_2} \quad (9)$$

$$k_s = \frac{k_{s1}h_1 + k_{s2}h_2}{h_1 + h_2}$$

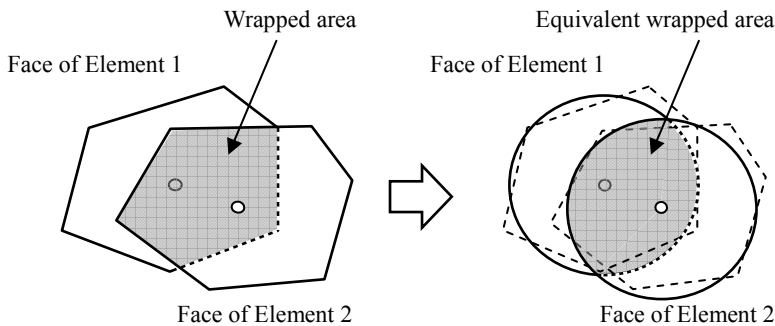


Fig. 8 Calculation of wrapped area.

where subscripts 1 and 2 represent elements 1 and 2 in Fig. 1, respectively.

After the crack occurrence or the yielding of shear spring, interface behavior governs the behavior of the spring. Constitutive models similar to those of the spring between mortars are applied to the interface springs. For the normal spring, the constitutive model in Fig. 5 is adopted. For the interface spring,  $w_{max}$  is set 0.0025mm for 3D analysis. In 2D RBSM analysis, it is 0.01mm where the fracture propagation in interface is presented by the line along the interface. In contrast, the fracture propagates leaving three-dimensionally spread fracture surface in the 3D analysis, which is the actual behavior. Hence it is considered that the fracturing area of interface is smaller in the 2D analysis. Then the smaller value of  $w_{max}$  is given in the 3D analysis. For shear springs, an elasto plastic model as shown in Fig. 6 is applied. The  $\tau_{max}$  criterion for the interface as shown in Eq. (10) and Fig. 9 is adopted.

$$\tau_{max} = \pm(-\sigma \tan \phi + c) \quad (\sigma \leq f_{elem}) \quad (10)$$

where  $\phi$  and  $c$  are constant values. This criterion is based on the failure criterion suggested by Taylor and Broms (1964) and Kosaka *et al.* (1975), which is derived from experimental results. Similarly to the spring between mortars, when fracture happens in normal spring, the calculated shear stress is reduced according to the reduction ratio of normal stress.

Similarly to the mortar model, stresses are transferred only through an over-wrapped part on the boundary faces after the stresses reach the  $\tau_{max}$  criterion (see Fig. 8).

## 4. Input material properties

In this study, numerical simulation of failure of normal concrete is carried out. For the simulation, the material properties of mortar, aggregate and interface between mortar and aggregate have to be introduced as input data (see Chapter 3). Some values of these material properties are not independent but affect each other. Therefore a method for determining the input material properties is developed based on a previous experiment, which is described minutely in the author's previous study (Nagai *et al.* 2004).

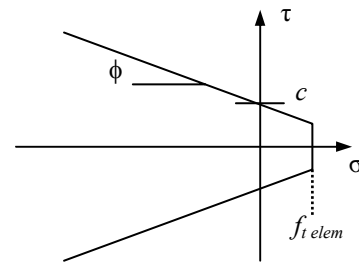


Fig. 9  $\tau_{max}$  criterion for interface.

**Figure 10** shows the developed flowchart for determining relationships between input material properties. Using the flowchart, the necessary material properties for the simulation, elastic modulus of mortar ( $E_m$ ), pure tensile strength of mortar ( $f_{tp}$ ), value of constant ( $c$ ) in the  $\tau_{max}$  criterion for interface (see Eq. (9) and **Fig. 10**) and tensile strength of interface ( $f_{ti}$ ) can be calculated from the target compressive strength of mortar ( $f'_{cm}$ ). The applicable range of the compressive strength of mortar is from 10 MPa to 65 MPa. However the value of  $f'_{cm}$  itself is not introduced in the simulation (see Chapter 3). The equations, which relate the material characteristics, are as follows.

$$E_m = 1000\{7.7 \ln(f'_{cm}) - 5.5\} \quad (11)$$

$$f_{tp} = 1.4 \ln(f'_{cm}) - 1.5 \quad (12)$$

$$C/W = 0.047 f'_{cm} + 0.5 \quad (13)$$

$$c = -2.6 W/C + 3.9 \quad (14)$$

$$f_{ti} = -1.44 W/C + 2.3 \quad (15)$$

where the  $W/C$  is water cement ratio. The tensile strengths of mortar ( $f_{tp}$ ) and interface ( $f_{ti}$ ) calculated in this chapter are applied as the average tensile strength ( $f_{t \text{ average}}$ ) of the component at the meso level in Chapter 3.

In addition, the elastic modulus of aggregate ( $E_a$ ), Poisson's ratio of mortar ( $\nu_m$ ) and aggregate ( $\nu_a$ ) and  $\phi$  for the interface  $\tau_{max}$  criterion must be provided in the simulation. Sufficient research on the values of  $E_a$ ,  $\nu_m$  and  $\nu_a$  has not yet been carried out, therefore the general values of 50 GPa, 0.18 and 0.25, respectively, are adopted in all the simulations. Regarding the value of  $\phi$ , due to the difficulty of clarifying the quantitative relationship from the previous studies (Taylor and Broms 1964; Kosaka *et al.* 1975), a typical value of  $35^\circ$  is applied to all the simulations.

## 5. Analysis of mortar

### 5.1 Compression and tension test

Numerical analyses of mortar specimens in uniaxial compression and tension are carried out. **Figure 11** shows 3D view of the analyzed specimen and the  $x$ - $y$

cross section at  $z = 35.0$  mm. The size of the specimen is  $70 \times 70 \times 140$  mm and the number of elements is 35,152. The average element size is  $2.69 \text{ mm}^3$ . The top and bottom loading boundaries are fixed in the lateral direction in the compression test and are not fixed in the tensile test. The target compressive strength of mortar is 35 MPa, so that the input material properties in simulation are calculated using the flowchart for determining input material properties (see Chapter 4). **Table 1** indicates the inputted values.

For the comparison with 3D analysis, compression and tension test of mortar specimen are analyzed by 2D RBSM. The size of specimen is  $70 \times 140$  mm as shown in **Fig. 12**. The average size of element, the material properties and the loading conditions are same as those of the 3D analysis. The number of element is 1,352. Since the results of 2D RBSM show variation (Nagai *et al.* 2004), the specimen that results the similar strengths in compression and tension to those in the 3D analysis is selected in this section.

**Figure 13** shows the predicted stress strain curve and the change of Poisson's ratio, which is called effective Poisson's ratio, in the compression test. Lateral strains are calculated by the relative deformation between the elements at A and B in **Figs. 11** and **12**. The strengths of the specimens are 35.77 MPa in the 3D analysis and 35.13 MPa in the 2D analysis. The target macroscopic compressive strengths of the specimens are predicted well by the simulations in which only tensile and shear failures are allowed at the meso scale. Similar stress strain curves in axial and lateral directions and the effective Poisson's ratio is predicted in the 3D and 2D RBSM analyses until the peak. The predicted curves in compression show nonlinearity in the axial direction from around 50% of maximum stress. The ratio of the lateral strain to the axial strain starts increasing rapidly around 70% of maximum stress. These behaviors were also observed in the experiment of mortar compression test (Harsh *et al.* 1990; Globe and Cohen 1999). **Figure 14** shows the deformations when the stresses in post peak

Table 1 Input material properties of mortar.

$f_{t \text{ average}}$	3.48 MPa
Elastic modulus ( $E_m$ )	21,876 MPa
Poisson's Ratio ( $\nu_m$ )	0.18

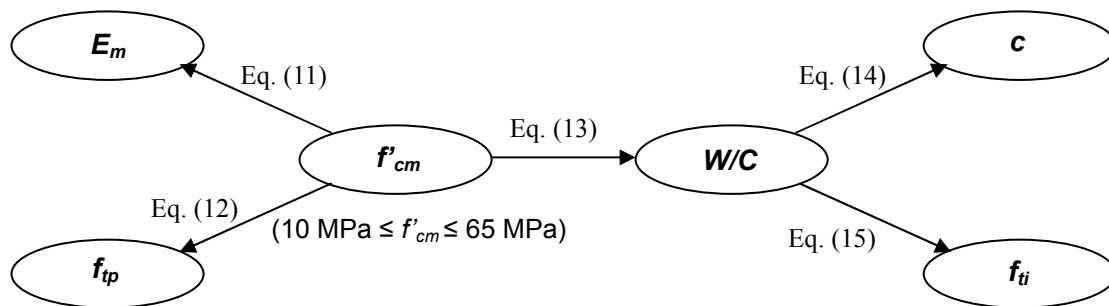
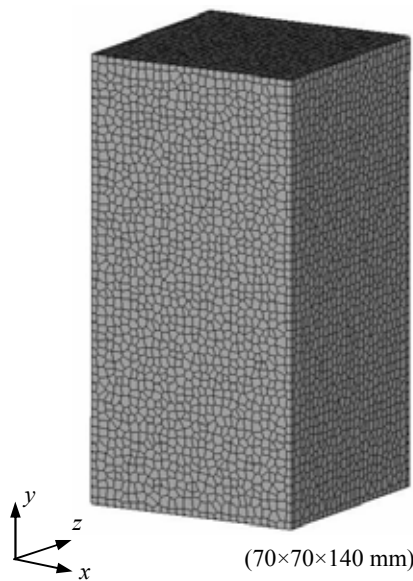


Fig. 10 Flowchart for determination of input material properties.



a) 3D view

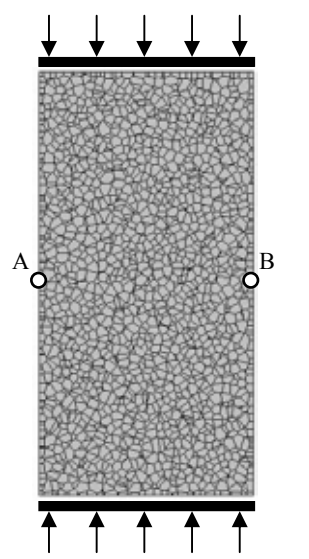
b) Cross section at  $z=35.0$  mm

Fig. 11 3D mortar specimen.

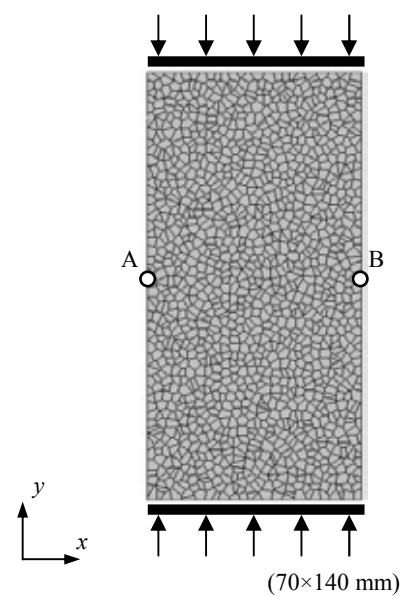


Fig. 12 2D mortar specimen.

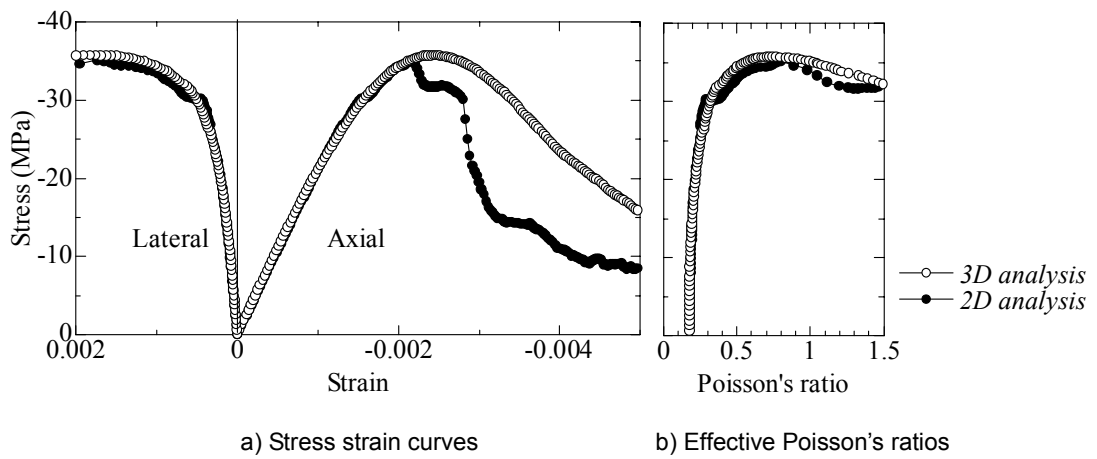
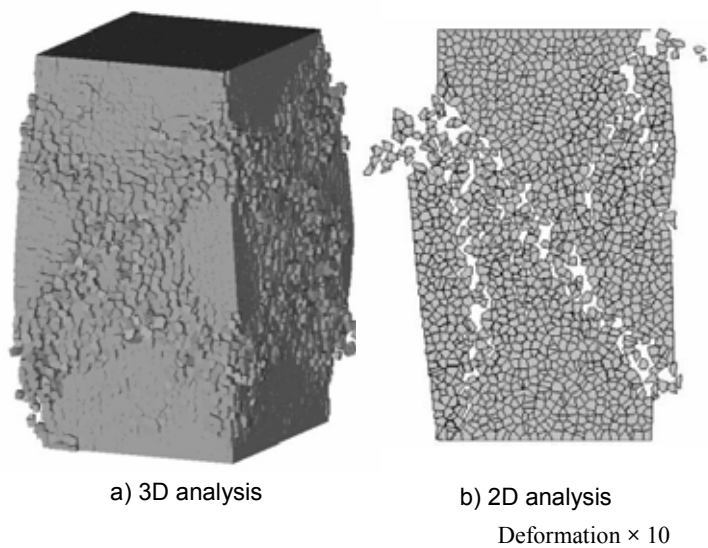


Fig. 13 Stress strain curves and Poisson's ratios.



a) 3D analysis

b) 2D analysis

Deformation  $\times 10$ 

Fig. 14 Deformation in compression at failure.

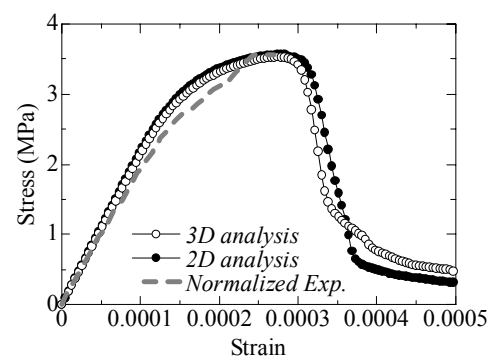


Fig. 15 Stress strain curve in tension.

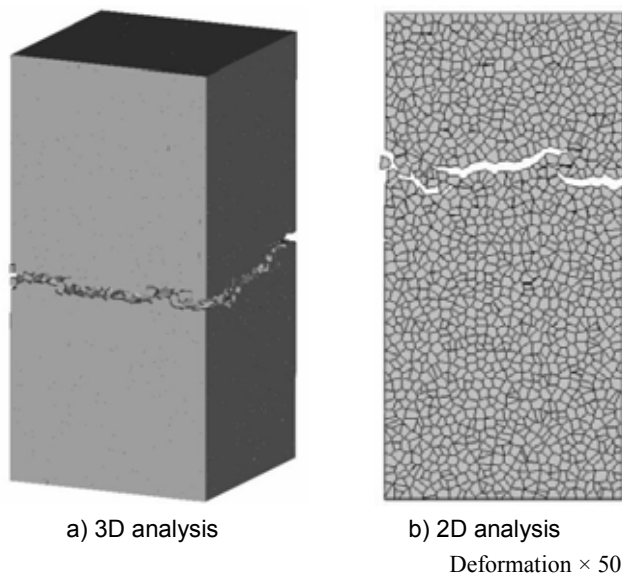


Fig. 16 Deformation in tension at failure.



Fig. 17 Cracked faces inside 3D specimen.

decrease to approximately 15 MPa. The strains are  $-5,000 \times 10^{-6}$  and  $-3,200 \times 10^{-6}$  in the 3D and 2D analyses, respectively. The deformations in  $x$ ,  $y$  and  $z$  directions are enlarged 10 times. The macro shear cracks emerge around the peak stress and propagate steadily to the failure as shown in Fig. 14 as observed in usual experiments.

Predicted stress strain curves in the tension analysis are presented in Fig. 15. The macroscopic tensile strengths of the 3D and 2D specimens are 3.57 MPa and 3.53 MPa, respectively, which also agree well with the given strength in tension (see Table 1). The simulated stress strain curves are similar. The shape of the curves shows nonlinearity before the peak stress as much as in compression. This behavior was observed in pure tensile testing of mortar (Gopalaratman and Shah 1985). The normalized stress strain curve in the experiment, in which the strength is 3.27 MPa, by peak stress and strain in the 3D analysis until the peak is presented in Fig. 15. Figure 16 shows the deformation of the model at failure (at strain of  $500 \times 10^{-6}$ ). The deformation is enlarged 50 times. The propagation of single crack that starts after the peak stress can be simulated as usually observed in experiments. Figure 17 shows cracked faces inside the 3D specimen whose crack widths reach 0.002 mm at the failure.

## 5.2 Relationship of strength in compression and tension

Analyses of uniaxial compression and tension test of mortar are carried out to examine the relationship between compressive and tensile strength. The same specimen as in Section 5.1 is analyzed. Target compressive strengths are set in 20 MPa, 35 MPa and 55 MPa. Conditions of loading boundaries are also same as in Section 5.1. The results in Section 5.1 are adopted as the

Table 2 Strength of mortar.

Target $f'_{cm}$ (set $f_t$ average)	Predicted strength	
	Compression	Tension
20MPa (2.69MPa)	19.43MPa	2.67MPa
35MPa (3.48MPa)	35.77MPa	3.57MPa
55MPa (4.11MPa)	54.45MPa	4.32MPa

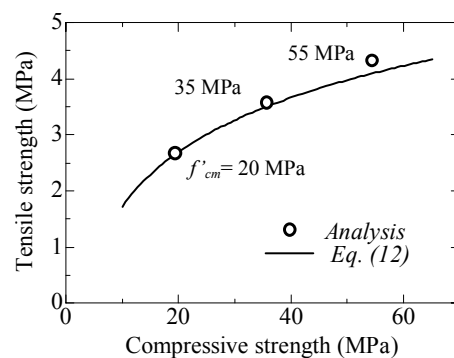


Fig. 18 Strength relationship of mortar.

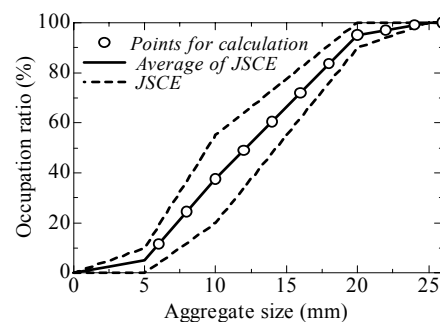


Fig. 19 Grain size distribution.



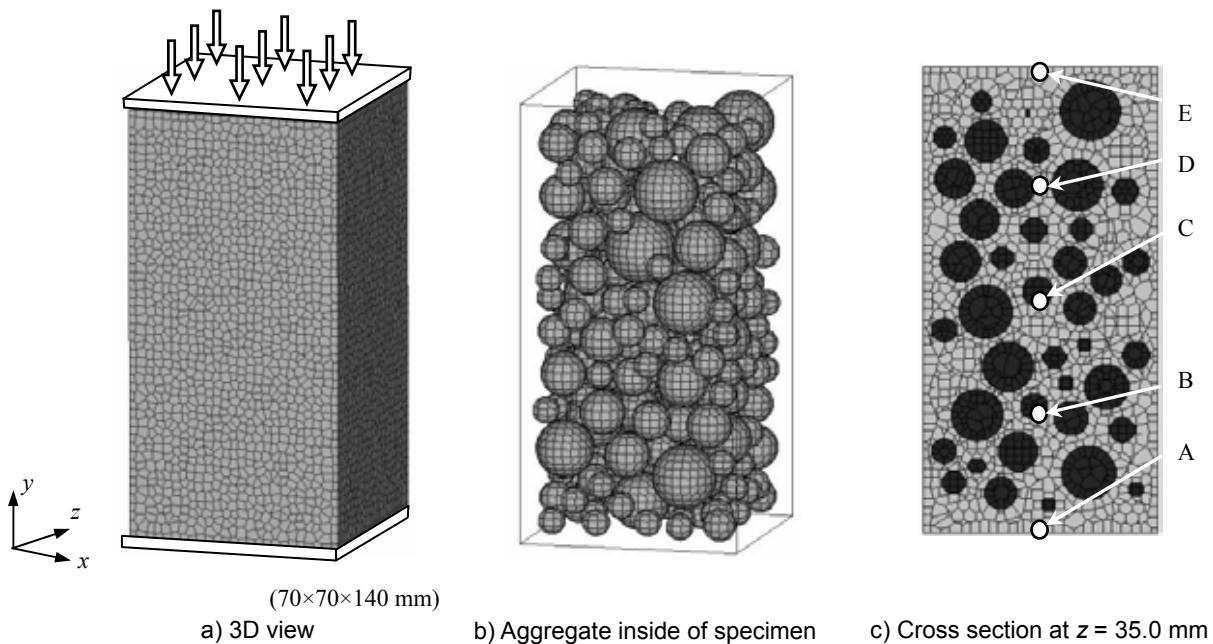


Fig. 20 3D concrete specimen.

Table 3 Introduced aggregate in 3D specimen.

Diameter (mm)	Number
8	121
10	62
12	31
14	20
16	13
18	9
20	7
22	1
Total	264

Table 4 Input material properties.

Mortar	
$f_{t \text{ average}}$	3.48 MPa
Elastic modulus ( $E_m$ )	21,876 MPa
Poisson's Ratio ( $\nu_m$ )	0.18
Aggregate	
Elastic modulus ( $E_a$ )	50,000 MPa
Poisson's Ratio ( $\nu_a$ )	0.25
Interface	
$f_{t \text{ average}}$	1.63 MPa
$c$	2.69 MPa
$\phi$	35°

analyses of specimen 35 MPa. The target strengths and the predicted strengths by simulations are presented in Table 2. Figure 18 shows the predicted compression and tension strength relationship of mortar. The analysis can simulate the target strengths and the strength relationship well although only the tensile strength is given as the input material strength in the analysis.

## 6. Analysis of uniaxial test of concrete

Simulations of failure of concrete under uniaxial compression and tension conditions are conducted in this chapter. The shape of the coarse aggregate in the concrete is spherical. The effect of the shape of aggregate is not discussed but will be studied in the future. Same way as in 2D RBSM analysis (Nagai *et al.* 2004) is adopted to determine the size and number of aggregate. Aggregate size distribution is determined based on the JSCE Standard Specification for Concrete Structures (2002a) and the maximum aggregate size is 20 mm as shown in Fig. 19. Aggregate diameters used for the analysis are varied

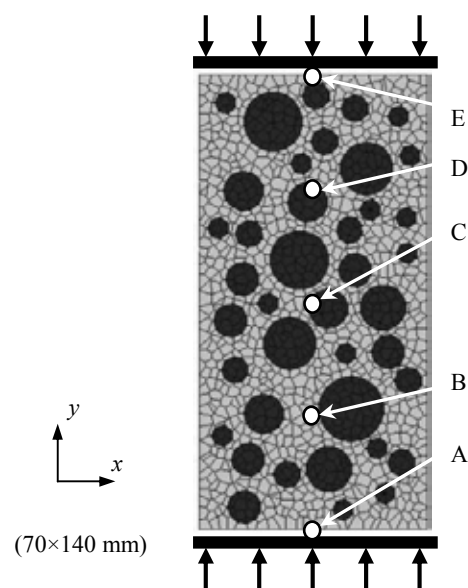


Fig. 21 2D concrete specimen.

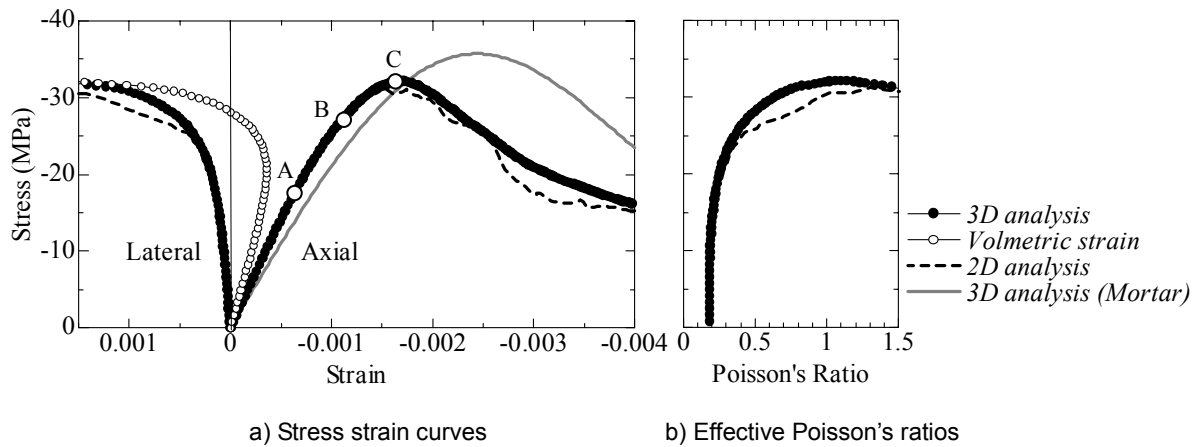


Fig. 22 Stress strain curves and effective Poisson's ratios of specimen B-FIX.

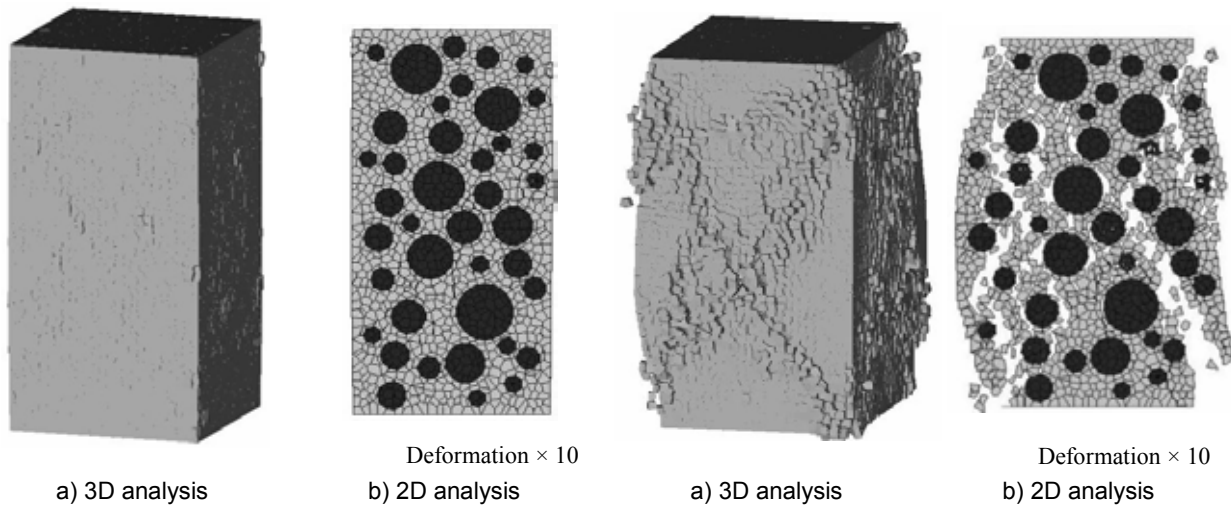


Fig. 23 Deformation of specimen B-FIX at peak stress.

Fig. 24 Deformation of specimen B-FIX at failure.

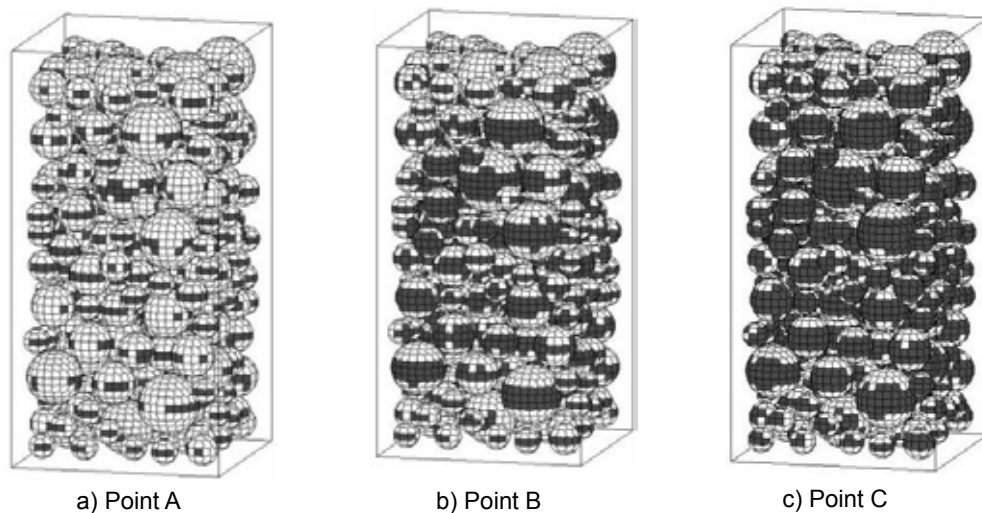


Fig. 25 Change of interface crack (B-FIX).

with 2 mm increments. The number of the aggregates of each size is calculated using the distribution curve in Fig. 19 and the points on the curve indicate the selected di-

ameters. However, due to the difficulty of forming sphere shape with the small size, the aggregates whose diameters are 6 mm are eliminated. Hence the aggregate vol-

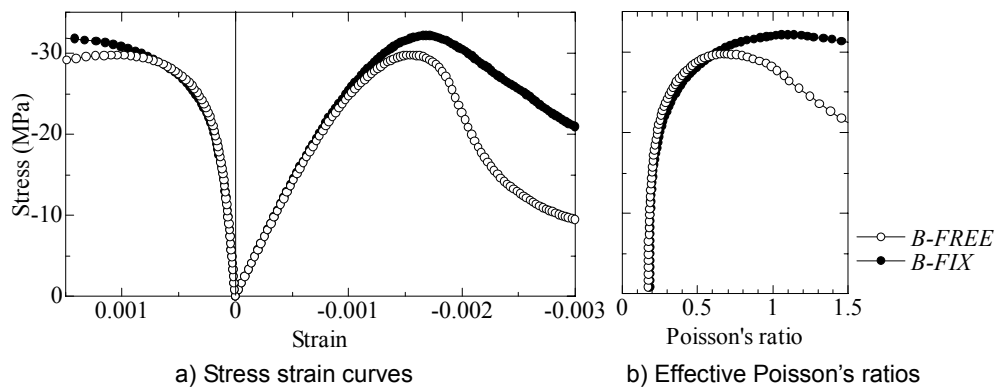


Fig. 26 Stress strain curves and effective Poisson's ratios.

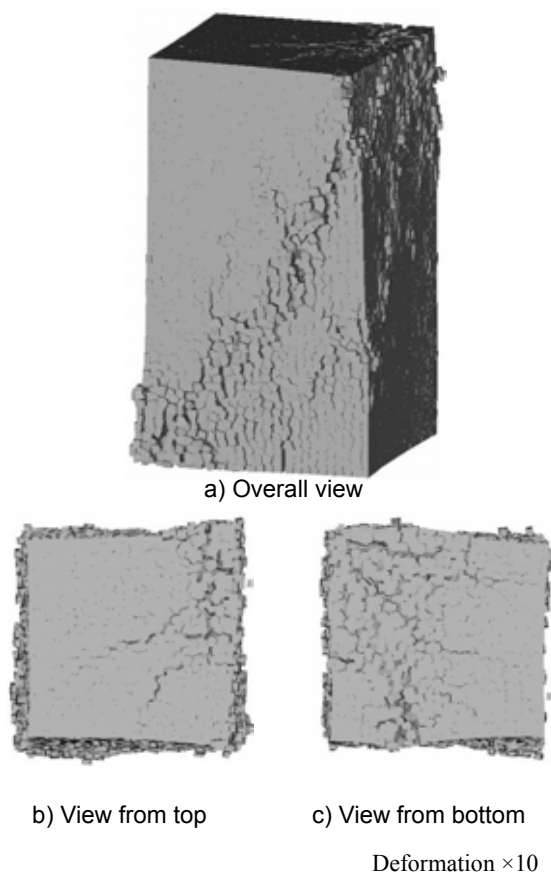


Fig. 27 Deformation of specimen B-FREE at failure.

ume in the specimen becomes lower than that in usual concrete. Target aggregate volume is approximately 35% therefore it becomes around 30% in the analysis.

### 6.1 Compression and tension test

Figure 20 shows an analyzed specimen ( $70 \times 70 \times 140$  mm) where the number of element is 39,162 including 17,082 elements of aggregate. Average element size is  $2.60 \text{ mm}^3$ . Aggregate volume in the specimen is 30.9%.

If the aggregates of 6 mm diameter could be introduced, it would become 34.9%. Table 3 shows the number of aggregate for each aggregate diameter and total number of aggregate. To examine the effect of loading boundary condition in the compression test, 2 types of models are analyzed: (i) Model where the top and bottom boundaries are fixed in the lateral direction (B-FIX); and (ii) Model where the boundaries are not fixed in the lateral direction (B-FREE). In the tension test, the loading boundaries in the lateral direction are not fixed. The target compressive strength of mortar is 35 MPa and the input material properties are determined by the flowchart in Chapter 4. The calculated values are indicated in Table 4.

For comparison with the 3D analysis, 2D RBSM analyses of concrete specimens are conducted. The size of specimen is  $70 \times 140$  mm as shown in Fig. 21. The number of element is 1,522 and the average size of element is  $2.54 \text{ mm}^2$ . Aggregate volume in the specimen is 33.7%. The material properties and the loading conditions are same as those of the 3D analysis. Since the results of 2D RBSM show variation in the peak stress (Nagai *et al.* 2004), the specimen that shows the similar strengths in compression and tension to those in the 3D analysis is selected in this section.

The predicted stress-strain and stress-effective Poisson's ratio relationships of specimens B-FIX are shown in Fig. 22. Stress-volumetric strain relationship in the 3D analysis and the result of mortar compression test in Section 5.1 are also presented. To calculate the lateral strain and volumetric strain, relative displacements of the elements at the center of side surface of the specimen are used. The predicted curves are similar in the 3D and 2D analyses where the strengths are 32.15 MPa and 31.26 MPa, respectively. Compared with the result of mortar specimen, reduction of strength due to the introduction of aggregates is simulated, which is observed in experiment (Christensen and Nielsen 1969; Kosaka *et al.* 1975; Stock *et al.* 1979). Natures of the curves of stress-strain, stress-effective Poisson's ratio and stress-volumetric strain relationships are similar to the experimental results mentioned by Stock *et al.* (1979) and Kosaka and Tani-

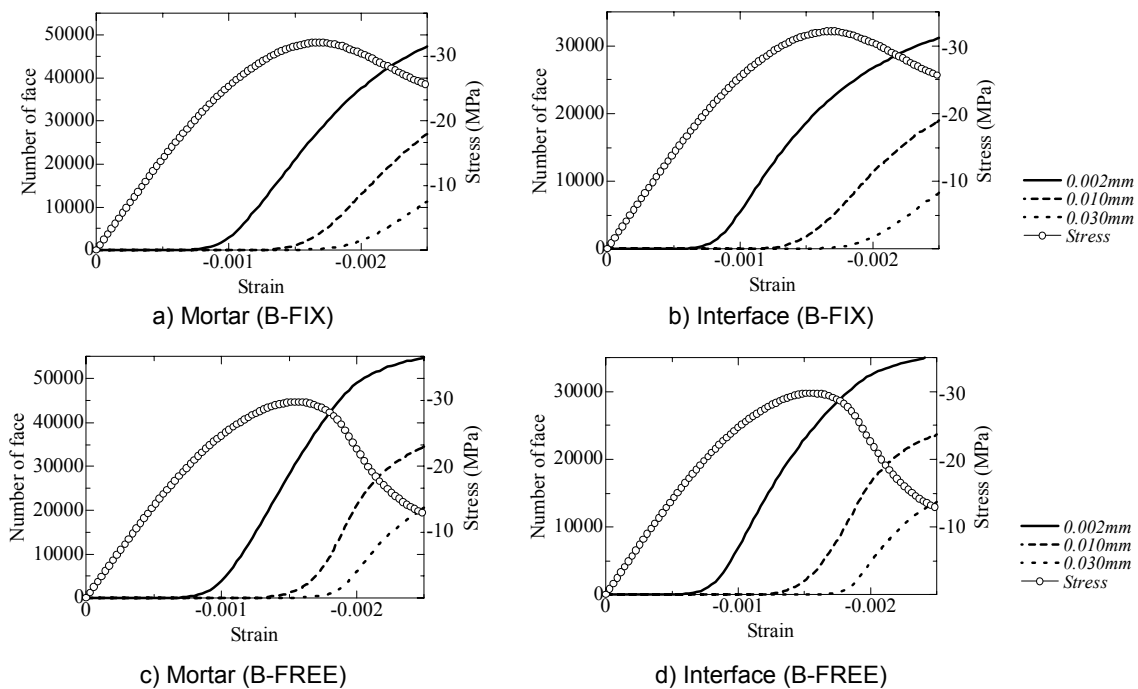


Fig. 28 Number of faces reaching certain crack width.

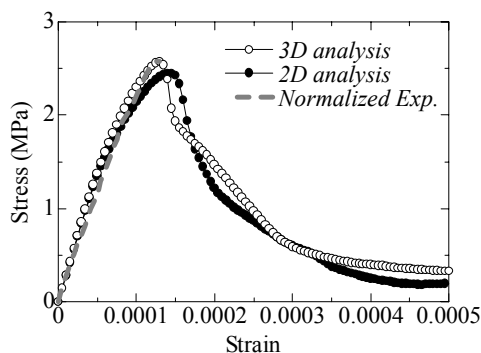


Fig. 29 Stress strain curves in tension.

gawa (1975a). **Figure 23** shows deformations of specimens at the peak stress. **Figure 24** shows the deformations when the stresses in post peak decrease to approximately 15 MPa. The deformations in  $x$ ,  $y$  and  $z$  directions are enlarged 10 times. At the peak stress, macro major cracks, which cause the failure of model, have not been developed visually yet. The macro shear cracks emerge around the peak stress and propagate steadily until the failure as shown in **Fig. 24** as observed in usual experiments. **Figure 25** shows change of interface condition of the 3D specimen at points A-C in **Fig. 22**. Black face indicates cracked interface. Development of crack band on the side of aggregate is simulated, while the top and bottom sides of aggregate do not have cracks. This local behavior on the aggregate surface is observed in the experiment (Christensen and Nielsen 1969; Kosaka *et al.* 1975; Kosaka and Tanigawa 1975b).

**Figure 26** shows the predicted curves of stress-strain and stress-effective Poisson's ratio relationships of

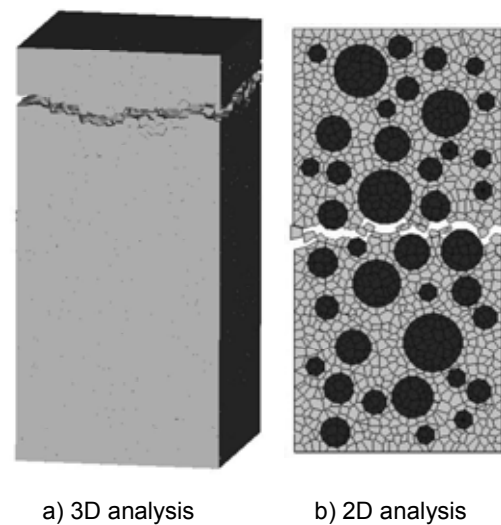


Fig. 30 Deformation at failure in tension.

specimen B-FREE and B-FIX. The macroscopic strength of specimen B-FREE is 29.74 MPa. Nature of the curve of specimen B-FREE is similar to that of B-FIX. A slight reduction in macroscopic strength due to the elimination of friction on the loading boundary is observed in the analysis, similarly to the experiment (Kosaka and Tanigawa 1969; Kosaka and Tanigawa 1975a; Matsushita *et al.* 1999). The curves of effective Poisson's ratio of specimens B-FIX and B-FREE agree well until around the peak stress of specimen B-FREE. However the loading boundary of specimen B-FREE cannot restrict the expansion of the specimen in the lateral direction. As

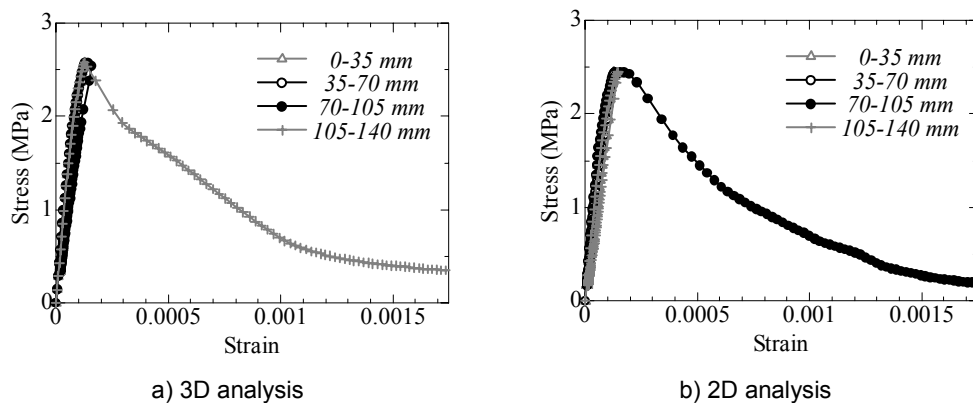


Fig. 31 Strain at every 35mm in axial direction.

a result the specimen B-FREE fails just after the rapid increasing of effective Poisson's ratio. This behavior is observed in the experiment and mentioned by Kosaka and Tanigawa (1975a). Failure deformations of the specimen B-FREE are shown in **Fig. 27** (at axial strain of  $-2,500 \times 10^{-6}$ ). The longitudinal main cracks reaching the loading boundary in specimen B-FREE is predicted, which is different from specimen B-FIX. This difference in crack pattern is observed in the experiment (Matsushita *et al.* 1999). The curves in **Fig. 28** show the numbers of faces where springs are set in mortar and interface between mortar and aggregate where the crack width reaches 0.002 mm, 0.01 mm and 0.03 mm in specimens B-FIX and B-FREE. Horizontal axes show the macroscopic strain of specimens. The macroscopic stresses of the specimens are presented together in the figures. Both specimens fail after the rapid increase in mortar and interface cracks. This is similar to the usual experimental results (Kato 1971; Kosaka and Tanigawa 1975b). The increase in the number of cracks reaching a certain crack width around the peak stress is more rapid in specimen B-FREE than in specimen B-FIX. This indicates that rapid propagation of cracks takes place in specimen B-FREE as the result of the free loading boundary. This

behavior is presented experimentally by Kotsovos (1983).

**Figure 29** shows the predicted stress strain curve in the tension tests. The strength of the specimen in 3D and 2D analyses are 2.57 MPa and 2.45 MPa, respectively. The nonlinearity in the predicted stress strain curves before peak stress is observed in the pure tension test in the experiment (Gopalaratnam and Shah 1985). The normalized stress strain curve in the experiment, in which the strength is 3.64 MPa, by peak stress and strain in the 3D analysis until the peak is presented in **Fig. 29**. Deformations of the models at failure are presented in **Fig. 30** (at strain of  $500 \times 10^{-6}$ ). The deformation is enlarged 50 times. As observed in usual experimental results (Ueda *et al.* 1993), the propagation of single crack

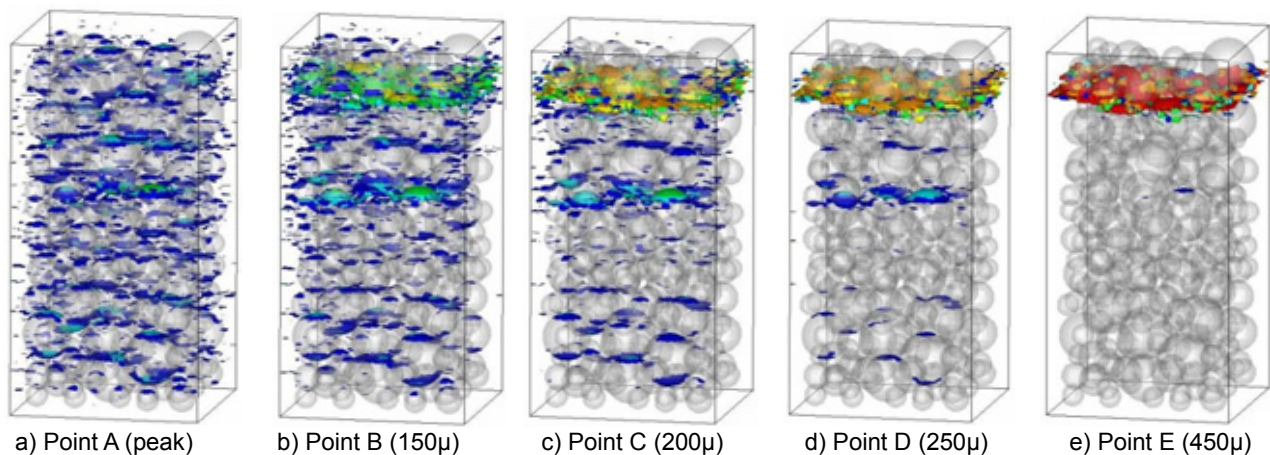
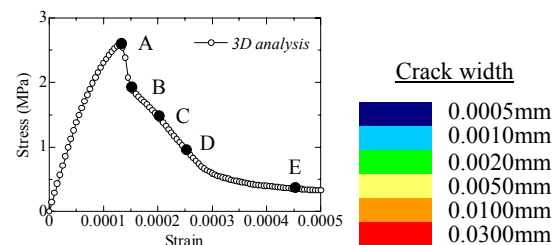


Fig. 32 Crack faces inside specimen in tension.

can be simulated. **Figure 31** shows the average strains of every 35 mm section in the axial direction. To calculate the strains of sections 0-35 mm, 35-70 mm, 70-105 mm and 105-140 mm in **Fig. 31**, relative deformations between the elements at A and B, B and C, C and D and D and E, respectively, in **Figs. 20** and **21** are used. The vertical axis shows the macroscopic stress. Until the peak, similar curves are predicted for each section in both 3D and 2D analyses. This means that the models elongate uniformly. In the post peak range, only the strains of the part where the macroscopic single cracks take place (see **Fig. 30**) increase and the strains in other sections decrease. **Figure 32** shows the change of cracked faces where crack widths reach certain values in the 3D analysis. At the peak stress, cracked faces are spread widely inside the specimen. From the peak to failure, the major single crack develops gradually and the cracks in other parts close. This localization behavior in failure processes in tension is also observed in usual experimental results.

These behaviors of concrete under uniaxial stress condition are simulated in 2D RBSM analysis as well (Nagai *et al.* 2004).

## 6.2 Relationship of strength in compression and tension

As given in the mortar analysis, the relationship between compressive and tensile strength of concrete is examined by the uniaxial compression and tension test. The same specimen as in Section 6.1 is analyzed. Target compressive strengths of mortar are 20 MPa, 35 MPa and 55 MPa. The loading boundaries in lateral direction are fixed in compression test and not fixed in tension test. The results in Section 6.1 are adopted as the analyses of specimen 35 MPa. Stress strain relations in **Fig. 33** show predicted curves in the compression and tension analyses until the peak stress. **Figure 34** shows the predicted compression and tension strength relationship of concrete. The curve in the figure shows the strength relationship suggested by JSCE (2002b). This relationship is,

$$f_{tcs} = 0.23 f'_c{}^{2/3} \quad (16)$$

where  $f'_c$  and  $f_{tcs}$  are the compressive and splitting tensile strength of concrete, respectively. In the analysis, pure tensile tests are carried out, and therefore Eq. (16) is modified by the equation developed by Yoshimoto *et al.* (1983) for pure tensile strength, which is presented in **Fig.**

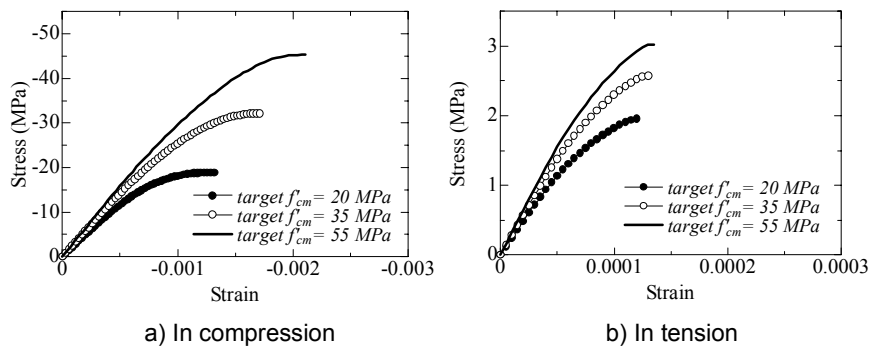


Fig. 33 Predicted stress strain relations.

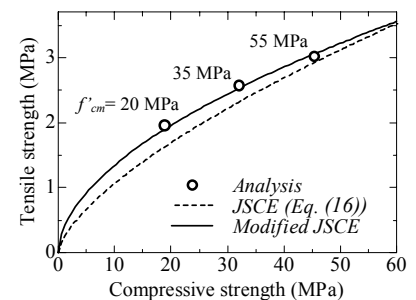


Fig. 34 Strength relations of concrete.

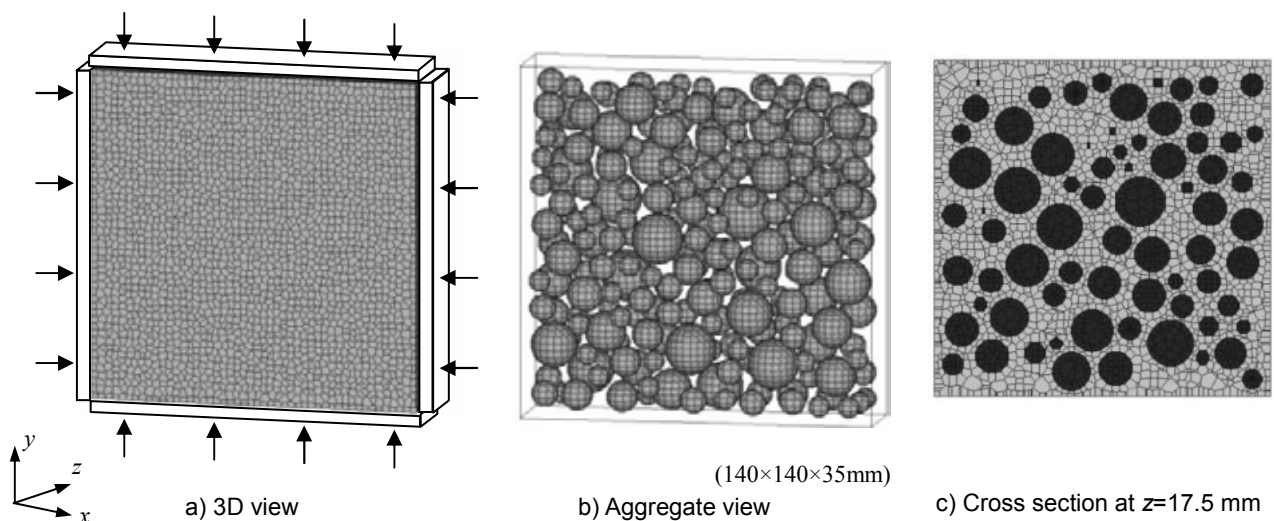


Fig. 35 3D specimen for biaxial test.



34. The analysis can simulate the strength relationship reasonably. The applicable compression strength of concrete in this analysis ranges approximately 20 to 45 MPa.

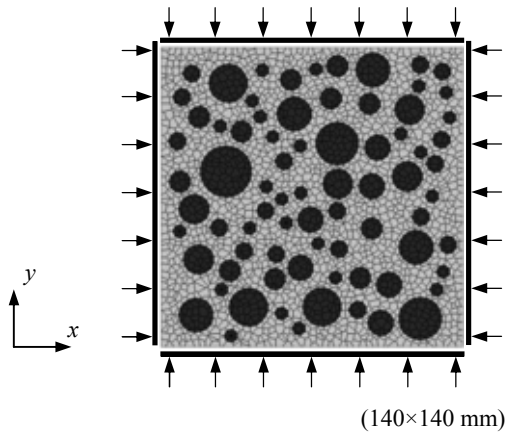


Fig. 36 2D specimen for biaxial test.

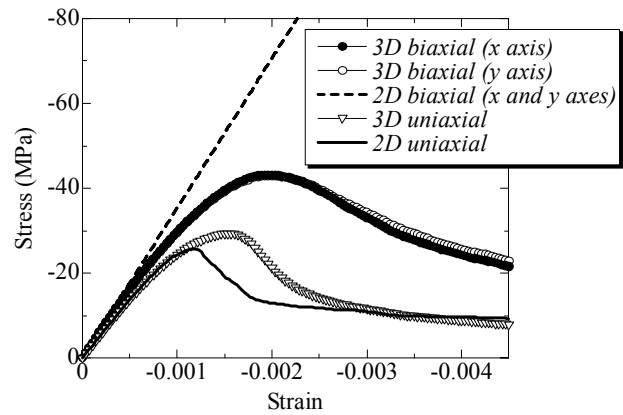


Fig. 37 Stress strain relationships.

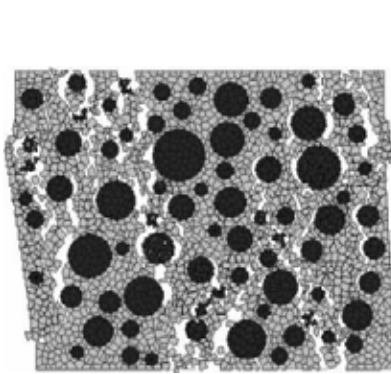
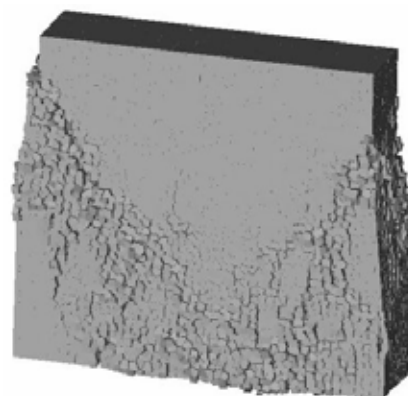
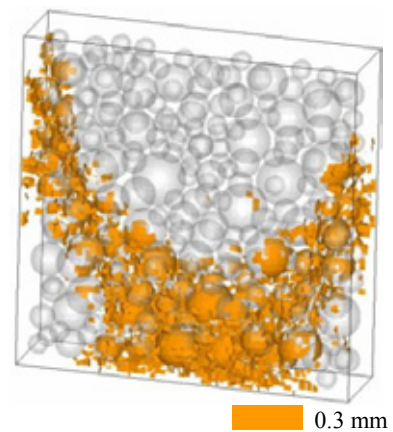


Fig. 38 Failure view (2D uniaxial test).



a) Failure view



b) Internal crack at failure

Fig. 39 Result of 3D uniaxial compression test.

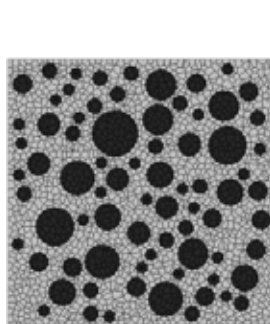
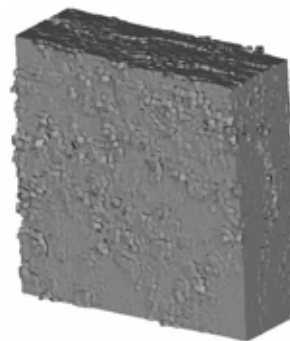


Fig. 40 Deformation at stress of 80 MPa (2D biaxial test).

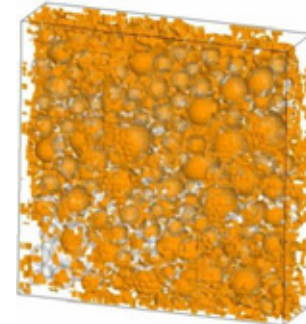


a.1) Whole view



a.2) From side

a) Failure view



b.1) Whole view



b.2) From side

b) Internal crack at failure

Fig. 41 Result of 3D biaxial compression test (Displacement ratio -1:-1).

## 7. Analysis of biaxial test of concrete

The fact that 2D RBMS mesoscopic analysis cannot simulate the behavior of concrete under biaxial compression stress condition is indicated in the author's

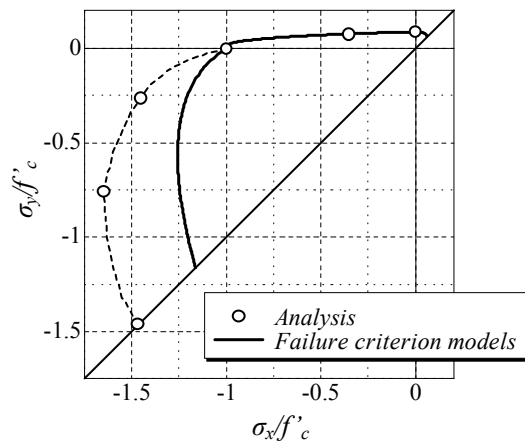


Fig. 42 Failure criterion under biaxial stress.

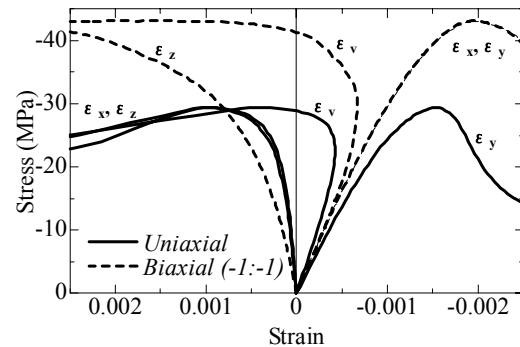


Fig. 43 Stress strain curves in 3D analyses.

previous research (Nagai *et al.* 2004). It is because the analysis cannot present the fracture in the normal direction to the plane of the specimen. In this chapter, analyses of concrete under biaxial stress condition by 3D RBSM are conducted.

**Figure 35** shows specimen for the analysis: overall view, aggregates inside the specimen and cross section in  $x$ - $y$  plane. The size of the specimen is  $140 \times 140 \times 35$  mm and the number of the element is 34,535. The average element size is  $2.71 \text{ mm}^3$ . The aspect ratio of the specimen is the same as in the experiment by Kupfer *et al.* (1969) though the size is smaller considering calculation time. The aggregate size and numbers are determined by the same way as in Chapter 6. Due to the difficulty of introduction of aggregates to the thin specimen in analysis, the aggregate volume becomes smaller than that of usual concrete, which is 27.9%. If the aggregates of 6 mm diameter could be introduced, it would become 31.5%. The simulation is conducted by displacement control of the loading boundaries. Friction between specimen and the loading boundaries is eliminated. The target compressive strength of mortar is set 35 MPa.

For the comparison with biaxial compression tests by the 3D RBSM (displacement ratio -1:-1), two-dimensional analyses are carried out. The analyzed specimen is shown in **Fig. 36**. The size of the specimen is  $140 \times 140$  mm and the number of elements is 2,917. The aggregate volume is 33.6% and the target strength and condition of loading boundaries are the same as those in the 3D specimen.

Stress strain curves in **Fig. 37** show the predicted results of analyses of uniaxial and biaxial (displacement ratio -1:-1) compression tests. In the uniaxial tests, although strength in the 2D analysis is lower than that in the 3D analysis, similar curves are simulated. **Figures 38 and 39** show deformations of the 2D and 3D specimens at strain of  $-4,500 \times 10^{-6}$ . The deformation is enlarged 5 times. Internal faces where the crack width reaches 0.3 mm at the same strain in the 3D specimen is presented in **Fig. 39**. Similar major crack bands forming at ap-

proximately 20~30 degrees with respect to the loading axis are simulated. In the biaxial test, only the 3D analysis predicts a peak stress. In the 2D analysis, the specimen behaves almost elastically. The deformation of 2D specimen at stress of 80 MPa is shown in **Fig. 40** where no fracture is observed because the analysis cannot simulate the crack in normal direction to the plane of the specimen. In contrast, normal cracks to the plane of the specimen are simulated in the 3D analysis as shown in **Fig. 41** where the deformation at strain of  $-4,500 \times 10^{-6}$  and the internal crack faces reaching 0.3mm width are presented. This crack pattern is different from that in the uniaxial test (see **Fig. 39**) but the same as observed in the experiment (Kupfer *et al.* 1969).

Some 3D analyses of biaxial test of concrete specimen in **Fig. 35** are carried out where the applying displacement ratios are varied, to examine the failure criterion. Predicted peak stresses normalized by uniaxial compressive strength are presented in **Fig. 42**, in which the criterion models of Kupfer in Compression-Compression (CC) domain (Kupfer *et al.* 1969), Niwa in Compression-Tension (CT) domain (Niwa *et al.* 1987) and Aoyagi and Yamada in Tension-Tension (TT) domain (Aoyagi and Yamada 1983) are drawn as well. The analysis predicts reasonably the criterion in CT and TT domain but overestimates the criterion in CC domain. However, the tendency of the criterion, such as the highest peak stress for around -0.5/-1 stress ratio, follows that of Kupfer model. It must be noticed that the analysis does not recreate exactly the same boundary condition of the experiment by Kupfer *et al.* (1969). The experiment was carried out by load control and the steel brush with high flexural stiffness was used for loading plate to reduce the friction.

**Figure 43** shows the stress-strain and stress-volumetric strain relationships in the 3D analyses of uniaxial and biaxial (displacement ratio -1:-1) compression tests. The strains are calculated using the relative deformations of the elements on the surface of specimen. In the uniaxial analysis, the specimen comes



to failure just after the volumetric strain change becomes increase from decrease. On the other hand, the stress increases by more than 10 MPa after the volumetric strain starts to increase in the biaxial analysis. In the experiment, specimen fails just after the volumetric strain starts to increase in both cases (Kupfer *et al.* 1969). This means that the fracture in normal direction to the plane of specimen dose not propagate smoothly around the peak stress in the analysis. The difference, which is the cause of overestimation of failure criterion, is necessary to be investigated considering the effect of loading boundary condition in the future.

## 8. Conclusions

The three-dimensional meso scale analyses of mortar and concrete by Rigid Body Spring Model (RBSM) are carried out in this study, which is necessary for the quantitative evaluation of behavior of concrete especially in compression and for the consideration of the environmental effect in the future. The following conclusions are drawn from the results of analyses despite the fact that the analysis still contains some assumptions which need further investigation.

- (1) In compression tests of mortar, macroscopic compressive strength is well predicted by the meso scale analysis where no compression failure at meso scale is assumed. The calculated stress strain curve shows a similar shape to that in usual experimental results.
- (2) In compression tests of concrete, predicted stress-strain and -volumetric strain curves and changes in Poisson's ratio are similar to those in experiments. Different crack patterns due to the difference in fixing condition of loading boundary can be simulated reasonably. The different incremental tendency of the number of cracks at meso scale around the peak stress is predicted.
- (3) Reduction in macro compressive and tensile strengths of the concrete due to the inclusion of aggregates can be predicted.
- (4) The analysis predicts well the compressive and tensile strength relationship of both mortar and concrete.
- (5) Localization of failure after the peak stress and the propagation of a single crack can be simulated in the tension analysis of mortar and concrete.
- (6) The 3D RBSM analysis can simulate similar behavior to that by 2D RBSM analysis in uniaxial test of mortar and concrete.
- (7) The 3D analysis reasonably simulates the failure crack pattern of concrete under biaxial compression stress condition, which is characterized by crack in normal direction to the plane of specimen, while 2D analysis cannot. The crack pattern in 3D analysis is different from that in uniaxial compression test.
- (8) Failure criterion under biaxial stress condition predicted by the 3D analysis agrees reasonably with existing models in compression-tension and ten-

sion-tension domains but overestimates the Kupfer model in compression-compression domain. The different behavior in CC domain may be due to slower propagation of crack normal to biaxial stress plane in the analysis than in the experiment. Further investigation including the effect of loading boundary condition is necessary.

## Acknowledgement

This study was supported by the 21<sup>st</sup> Century COE program 'Sustainable Metabolic System of Water and Waste for Area-based Society' of Hokkaido University.

## References

- Aoyagi, Y. and Yamada, K. (1983). "Strength of deformation characteristics of reinforced concrete shell elements subjected to in-plane force." *Proceeding of JSCE*, 331, 167-180. (in Japanese)
- Bolander, J. E. and S. Berton, S. (2004). "Cohesive zone modeling of fracture in irregular lattices." *Proceedings of FraMCoS-5*, 989-994.
- Christensen, P. N. and Nielsen, T. P. H. (1969). "Modal deformation of the effect of bond between coarse aggregate and mortar on the compressive strength of concrete." *ACI Journal*, 66(1), 69-72.
- Cundall, P. A. and Strack, O. D. L. (1979). "A discrete numerical model for granular subassemblies." *Geotechnique*, 29, 47-65.
- Cusatis, G., Bazant, Z. P. and Cedolin, L. (2003a). "Confinement-shear lattice model for concrete damage in tension and compression: 1. Theory." *Journal of Engineering Mechanics*, 129(12), 1439-1448.
- Cusatis, G., Bazant, Z. P. and Cedolin, L. (2003b). "Confinement-shear lattice model for concrete damage in tension and compression: 2. Computation and validation." *Journal of Engineering Mechanics*, 129(12), 1449-1458.
- Goble, C. F. and Cohen, M. D. (1999). "Influence of aggregate surface area on mechanical properties of mortar." *ACI Materials Journal*, 96 (6), 657-662.
- Gopalratnam, V. S. and Shah, S. P. (1985). "Softening response of plain concrete in direct tension." *ACI Journal*, 82 (3), 310-323.
- Harsh, S., Shen, Z. and Darwin, D. (1990). "Strain-rate sensitive behavior of cement paste and mortar in compression." *ACI Materials Journal*, 87 (5), 508-516.
- JSCE (2002a). "Standard specification for concrete structures, Materials and construction." Tokyo: JSCE. (in Japanese)
- JSCE (2002b). "Standard specification for concrete structures, Structural performance verification." Tokyo: JSCE. (in Japanese)
- Kato, K. (1971). "Micro cracks and physical properties of plane concrete." *Proceedings of JSCE*, 188, 61-72. (in Japanese)
- Kawai, T. (1978). "New discrete models and their

- application to seismic response analysis of structure.” *Nuclear Engineering and Design*, 48, 207-229.
- Kawai, T. and Takeuchi, N. (1990). “Discrete limit analysis program, Series of limit analysis by computer 2.” Tokyo: Baifukan. (in Japanese)
- Kosaka, Y. and Tanigawa, Y. (1969). “Study on influence of size of specimen and friction of loading surface on compressive strength of various concrete.” *Cement Concrete*, Japan Cement Association, 265, 2-10. (in Japanese)
- Kosaka, Y. and Tanigawa, Y. (1975a). “Effect of coarse aggregate on fracture of concrete (part 3).” *Journal of AIJ*, 233, 21-32. (in Japanese)
- Kosaka, Y. and Tanigawa, Y. (1975b). “Effect of coarse aggregate on fracture of concrete (part 2).” *Journal of AIJ*, 231, 1-11. (in Japanese)
- Kosaka, Y., Tanigawa, Y. and Kawakami, M. (1975). “Effect of coarse aggregate on fracture of concrete (part 1).” *Journal of AIJ*, 228, 1-11. (in Japanese)
- Kotsovos, M. D. (1983). “Effect of testing techniques on the post-ultimate behavior of concrete in compression.” *Materials and Structures*, 16 (91), 3-12.
- Kupfer, H., Hilsdorf, K. H. and Rusch, H. (1969). “Behavior of concrete under biaxial stresses.” *ACI Journal*, 66(8), 656-666.
- Lilliu, G. and van Mier, J. G. M. (2003). “3D lattice type fracture model for concrete.” *Engineering Fracture Mechanics*, 70, 927-941.
- Matsushita, H., Tsuruta H. and Sue, Y. (1999). “Effect due to friction of loading surface on the uniaxial compression test.” *Cement Science and Concrete Technology*, Japan Cement Association, 53, 621-626. (in Japanese)
- Nagai, G., Yamada, T. and Wada, A. (1998). “Stress analysis of concrete material based on geometrically accurate finite element modeling.” *Proceedings of FraMCoS-3*, 1077-1086.
- Nagai, G., Yamada, T. and Watanabe, K. (2004). “3D-image-based finite element modeling of granular composites using discontinuous element and iso-surface reconstruction.” *Transactions of the Japan Society of Mechanical Engineers*, 70(691), 84-91. (in Japanese)
- Nagai, K. (2002). “Numerical simulation of fracture process of concrete model by Rigid Body Spring Method.” Thesis (Master of Eng.). Hokkaido University.
- Nagai, K., Sato, Y. and Ueda, T. (2004). “Mesoscopic simulation of failure of mortar and concrete by 2D RBSPM.” *Journal of Advanced Concrete Technology*, 2(3), 359-374.
- Niwa, J., Yamada, K., Yokozawa, K. and Okamura, H. (1987). “Revaluation of the equation for shear strength of reinforced concrete beams without web reinforcement.” *Concrete Library of JSCE*, 9, 65-84.
- Stock, A. F., Hannant, D. J. and Williams, R. I. T. (1979). “The effect of aggregate concentration upon the strength and modulus of elasticity of concrete.” *Magazine of Concrete Research*, 31 (109), 225-234.
- Taylor, M. A. and Brooms, B. B. (1964). “Shear bond strength between coarse aggregate and cement paste or mortar.” *Journal of the ACI*, 61 (8), 939-956.
- Toi, Y. and Kiyosue, T. (1995). “Damage mechanics model for brittle microcracking solids based on three-dimensional mesoscopic simulation.” *Engineering Fracture Mechanics*, 50(1), 11-27.
- Ueda, M., Hasebe, N., Sato M. and Okuda, H. (1993). “Fracture mechanism of plain concrete under uniaxial tension.” *J. Materials, Conc. Struct., Pavements*, JSCE, 19, 69-78. (in Japanese)
- Wang, M. L. and Chen, Z. (1998). “Experimental and numerical investigations of concrete failure under triaxial loading.” *Proceedings of FraMCoS-3*, 793-802.
- Yoshimoto, A., Hasegawa, H. and Kawakami, M. (1983). “Comparison of strength obtained from pure tension, split and bending tests of concrete and mortar.” *Cement Concrete*, Japan Cement Association, 435, 42-48. (in Japanese)